energies

MDPI

Article

Performance Evaluation of a Stator Modular Ring Generator for a Shrouded Wind Turbine

Jefferson A. Oliveira [1,*] and Ály F. Flores Filho [2]

[1] Institute of Agricultural and Technological Sciences, Mechanical Engineering, Federal University of Rondonópolis, Rondonópolis 78736-900, Brazil
[2] Engineering School, Electrical Engineering, Federal University of Rio Grande do Sul, Porto Alegre 90035-190, Brazil; aly.flores@ufrgs.br
* Correspondence: jefferson@ufr.edu.br

Abstract: This paper presents the performance evaluation of a stator modular ring permanent-magnet generator to be embedded in a shrouded wind turbine. That is done to increase the power conversion for the same turbine area when compared to more conventional ones. An adapted structure allows the assembling of the prototype, aiming to verify its performance under controlled conditions. Aiming to verify the accuracy of an analytical subdomain model for a large diameter machine, the evaluation compares the results obtained by the electromagnetic finite element method and experimental measurements. The results of the components of the air-gap flux density, back EMF and electromagnetic torque obtained by the proposed analytical model and finite-element method are in good agreement with the experimental measurements. The experimental measurements of the iron loss and copper loss show that the prototype efficiency can reach 90% approximately.

Keywords: wind generation; modular stator; performance evaluation; analytical model

Citation: Oliveira, J.A.; Filho, Á.F.F. Performance Evaluation of a Stator Modular Ring Generator for a Shrouded Wind Turbine. *Energies* **2021**, *14*, 67. https://dx.doi.org/10.3390/en14010067

Received: 2 November 2020
Accepted: 15 December 2020
Published: 25 December 2020

1. Introduction

Efforts to reduce pollutant emissions and the impact of global warming have led countries around the world to invest in renewable energy sources such as solar and wind. Despite the advantages of wind energy, there are still many challenges for further expansion of the energy matrix, including the development of more efficient generators. Aiming to increase renewable energy usage, residences and commercial buildings have been encouraged to produce their own clean energy. However, constant changes in the direction of the wind produce turbulence that reduces the efficiency of the turbine in urban environments. Therefore, the development of mechanisms that allow the integration of wind turbines in buildings is essential for the operation of a wind system in these conditions [1]. Among the alternatives studied to increase the wind power of turbines, the use of a wind concentrator that involves the turbine and increases the wind speed is proposed [2]. Studies of the dimensions and shape of the wind concentrator show that it is possible to obtain an increase in wind speed of up to 5 times when compared to a standard wind turbine [3].

To develop a wind system that can be applied in an urban environment that, in addition to operating at low wind speeds, provides security in relation to the possibility of the blades detaching, the insertion of a diffuser is a solution that meets these two requirements. Based on the concept of using the diffuser, the proposal to install the rotor of the electric generator in the tips of the turbine blades, in the form of a ring, and to insert the stator in the structure of the diffuser is presented by [4]. However, the construction of this kind of machine introduces an issue concerning the turbine diameter, and to reduce its complexity the proposal of stator modularization allows simplifying its manufacturing and assembling.

A comparison between the design of two wind generators, one a continuous core and the other with a modular stator, both with 400 kW power and 2.1 m rotor diameter, shows that the modular construction is more efficient at full load and has less mass of active material [5]. The comparison of a stator interior permanent-magnet generator (SIPMG) with power between 3 MW and 10 MW and internal diameter of the stator between 3.7 m and 9.7 m shows that the SIPMG has about 120% density torque and 78% of the cost per kilowatt compared to the conventional generator [6]. Another version developed connects each module of a flux-switching permanent-magnet generator to an electronic converter, where the total power is 450 kW, which allows the generator to continue operating even if one of the modules presents problems [7]. Recently, the concept of the modular stator has also been applied to the design of electric motors; however, in these cases the machines have diameters lower than 0.4 m and power lower than 3.5 kW [8–10].

In general, studies with a modular stator present machines in which the torque transmission is carried out by the machine shaft. In addition, wind generators with a modular stator are of large power, while small-power machines have smaller diameters. The wind generator with a modular stator presented in this paper has characteristics not yet evaluated, because despite having dimensions for a wind turbine for urban applications, it has a large diameter, 1.5 m, and a power of 1 kW. Figure 1 presents the structure of the small, shrouded wind turbine used to design the stator modular ring generator, with the permanent-magnet mounted surface evaluated in this paper.

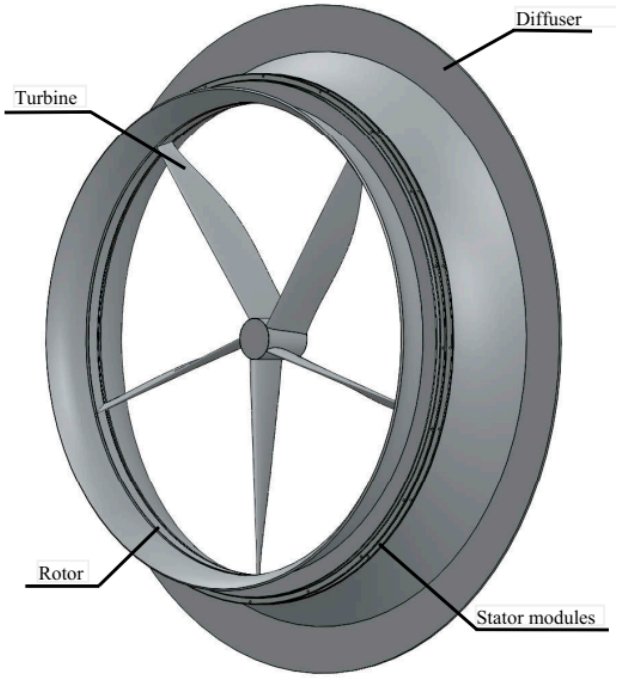

Figure 1. Shrouded wind turbine and stator modular ring generator.

This paper presents the electromagnetic performance evaluation of the generator as embedded in a small, shrouded wind turbine, tested under controlled conditions of rotation and load using a structure with the same dimensions as the wind turbine with diffuser and comparing the experimental results to analytical results obtained by means of a subdomain model and by a 2D finite element method (FEM). The stator modular ring generator aims to produce energy within the largest possible wind speed range in urban areas. The design of the generator aims to connect it to the grid through an AC/AC converter, and the performance evaluation considers the generation operation prior to its grid connection.

2. Methodology

The development of the synchronous generator with modular stator is based on the relationship between power and speed of rotation of a small wind turbine with diffuser. The design of the synchronous generator with modular stator evaluated different possibilities of modules and quantity of poles as a function of copper and iron losses [11]. The parameters of the synchronous generator with modular stator were evaluated experimentally [12]. The experimental tests provide the results of mechanical torque, terminal voltage and current for different speeds in the operating work range of the wind turbine. The results of the analytical modeling and the finite element method are compared with the experimental results to verify the accuracy of both methods. The following sections present the details of the wind generator with a modular stator.

2.1. Stator Modular Ring Generator Model

The performance evaluation considers as a reference the power and rotation of the wind turbine, calculated as

$$P_T = \frac{1}{2}\rho C_w V_w^3 A_T \quad (1)$$

where ρ is the air density, C_W is the power coefficient of the turbine, V_w is the wind speed and A_T is the area covered by the movement of the blades of the turbine. The application of Equation (1) leads to the graph presented in Figure 2, which shows the improvement of power of the shrouded wind turbine considering the power coefficient is equal to 0.4 and a wind speed augmentation of 1.5.

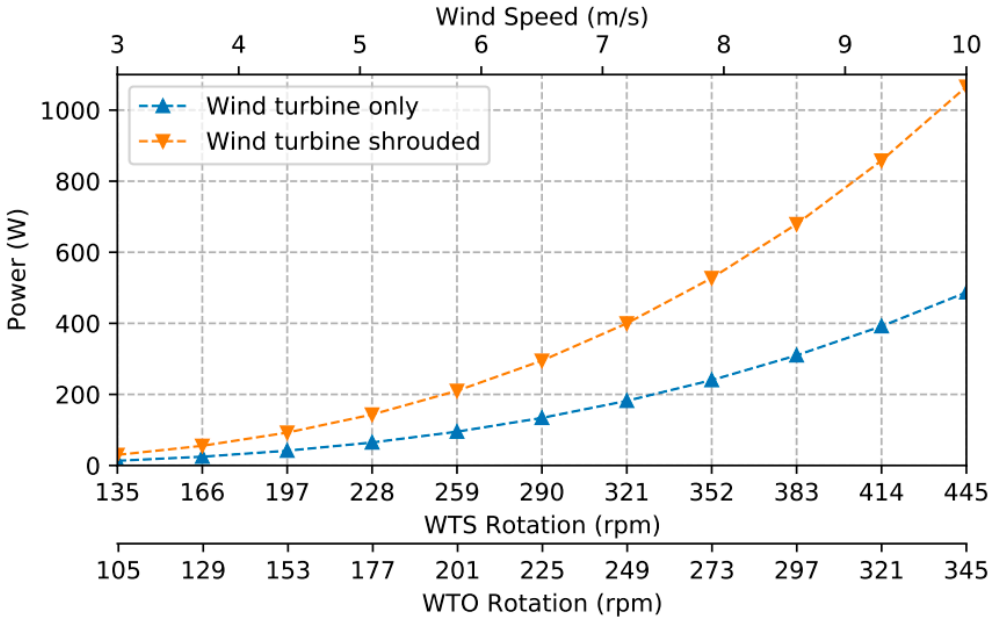

Figure 2. Wind turbine output power.

In this paper, the power curve of the shrouded wind turbine shows an increase of approximately 2.2 times in comparison to a standard wind turbine. As shown in Figure 1, the system structure uses mechanical parts to support the generator into the shrouded turbine. However, this study considers only the electromagnetic parts to develop the analytical model and the FEM simulation.

The stator modular ring generator is made of a rotor back iron with 40 poles of ferrite magnets and 20 stator modules with three phases each. Considering the circumference size and making proper use of the symmetries, a reduced electromagnetic model can be employed. Thus, the analytical model and FEM simulation consider the smallest symmetric fraction, which is 1/20 of the entire machine as shown in Figure 3.

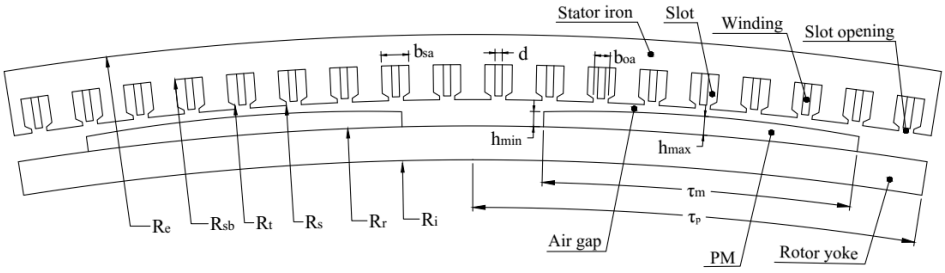

Figure 3. Stator module and a pair of pole model.

Table 1 presents the dimensions of the stator module of Figure 3.

Table 1. Main parameters of prototype generator (length unit: mm).

Parameters	Dimensions	Parameters	Dimensions
Stator outer diameter (R_e)	797	Pole-arc to pole pitch ratio (τ_m/τ_p)	0.7
Stator yoke height	6.7	Slot-width (b_{sa})	0.53
Stator inner diameter (R_S)	781	Slot-opening (b_{oa})	0.29
Tooth tip edge	1	Winding turn/phase	12
Magnet thickness (h_{max})	5	Axial length	20
Magnet thickness (h_{min})	4	Coercive force (kA/m)	212
Rotor outer diameter (R_r)	774	Magnetization	Parallel
Rotor inner diameter (R_i)	765	Winding-width (d)	0.29

The generator assembly connects stator modules in series. Hence, the results obtained in one fraction of the machine provide its performance multiplying by the total number of modules, as described in the sections that follow.

2.2. Analytical Model

An analytical subdomain model is the method employed to solve this problem due to its accuracy taking into account semiclosed slots under load conditions [13,14]. The analytical modeling considers the following assumptions:

- infinite permeable iron materials.
- nonconductive stator/rotor laminations.
- negligible end effect.
- uniform distributed current density in conductor area.
- relative permeability of the permanent magnets equals 1.
- opening slot and slots have radial sides.

This work presents the modeling with semi closed slots and the permanent magnets' eccentric shapes and armature reaction field using three regions, i.e., magnets and air gap (Region 1), slot openings (Region 2i, i = 1, 2, . . . ,18) and winding slots (Region 3i, i = 1,2, . . . ,18), according to Figure 3.

The model solution uses the magnetic vector potential obtained by

$$\frac{\partial^2 A_z}{\partial r^2} + \frac{1}{r}\frac{\partial A_z}{\partial r} + \frac{1}{r^2}\frac{\partial^2 A_z}{\partial \theta^2} = -\mu_0\left(\frac{M_\theta}{r} - \frac{\partial M_r}{\partial \theta}\right) \quad (2)$$

in the magnet subdomain,

$$\frac{\partial^2 A_z}{\partial r^2} + \frac{1}{r}\frac{\partial A_z}{\partial r} + \frac{1}{r^2}\frac{\partial^2 A_z}{\partial \theta^2} = 0 \quad (3)$$

in the air gap and slot opening and

$$\frac{\partial^2 A_z}{\partial r^2} + \frac{1}{r}\frac{\partial A_z}{\partial r} + \frac{1}{r^2}\frac{\partial^2 A_z}{\partial \theta^2} = -\mu_0 J \quad (4)$$

in the slots. The work of Wu et al. [14] presents the development of these equations conducting to an accurate result of flux density in the air gap. However, when the magnets have eccentric shapes it becomes harder to define the limits of the magnets' subdomain and consequently apply the interface condition with the air-gap subdomain. Intending to simplify the problem in this case, the magnet modeling by equivalent surface currents allows uniting the subdomains of magnet and air gap. The procedure to determine the equivalent surface currents consists of [15]:

$$\vec{J} = \vec{M} \times \vec{n_s} \tag{5}$$

where $\vec{n_s}$ is a normal vector of the evaluated surface as shown in Figure 4.

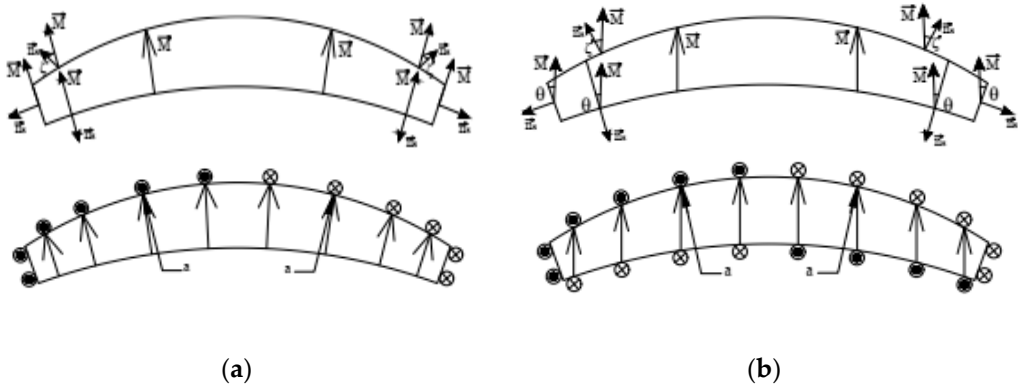

(**a**) (**b**)

Figure 4. Permanents magnets eccentric shapes models with: (**a**) radial magnetization; (**b**) parallel magnetization.

When modeling permanent magnets with equivalent surface currents, the particular solution of this subdomain is the following [16]:

$$A_p = \frac{\mu_0 i_c}{\pi}\left[\ln r \pm \sum_m \frac{1}{m}\left(\frac{a}{r}\right)^m cos(m(\theta \pm \zeta))\right] \tag{6}$$

when $a > r$ and

$$A_p = \frac{\mu_0 i_c}{\pi}\left[\ln r \pm \sum_m \frac{1}{m}\left(\frac{r}{a}\right)^m cos(m(\theta \pm \zeta))\right] \tag{7}$$

when $r > a$, where i_c is the current of the equivalent coil of each permanent-magnet side and ζ is the angle between the current of the equivalent coil and the evaluated point. Zhou et al. [17] present the solution to the equation for the region of the permanent magnets and air gap, applying the boundary condition of rotor yoke as well as the equations' description of eccentric permanent-magnet shapes for open slots. Semi closed slots with permanent magnets' eccentric shapes, without winding currents, are presented in [18]; meanwhile, a model that predicts an armature reaction field with permanent magnets' concentric shapes is calculated in [19]. The governing equations' solutions, after applying the boundaries conditions of each subdomain are:

$$\begin{aligned} A_{z1} = A_{11}(r^m + \frac{R_r^{2m}}{r^m})\cos(m\theta) \\ + \left[C_{11}\left(r^m + \frac{R_r^{2m}}{r^m}\right) + \frac{\mu_0 i_c}{m\pi a^m}\left(r^m + \frac{R_r^{2m}}{r^m}\right)\sin(m\zeta)\right]\sin(m\theta) \end{aligned} \tag{8}$$

for permanent magnet and air-gap subdomain,

$$A_{z2i} = A_{20} + B_{20}\ln r + \left(A_{21}r^{E_n} + \frac{B_{21}}{r^{E_n}}\right)\cos\left(E_n\left(\theta + \frac{b_{oa}}{2} - \theta_i\right)\right) \tag{9}$$

for slot opening, where

$$E_n = \frac{n\pi}{b_{oa}} \tag{10}$$

and

$$\begin{aligned} A_{z3i} = A_{30} + \frac{\mu_0 J_0}{4}\left[2R_{sb}^2 \ln r - r^2\right] \\ + \left[A_{31}\left(r^{E_k} + \frac{R_{sb}^{2E_k}}{r^{E_k}}\right) + \frac{\mu_0 J_k}{E_k^2 - 4}\left(r^2 + \frac{2R_{sb}^{2+E_k}}{E_k r^{E_k}}\right)\right]\cos\left(E_k\left(\theta + \frac{b_{sa}}{2} - \theta_i\right)\right) \end{aligned} \tag{11}$$

where

$$E_k = \frac{n\pi}{b_{sa}} \tag{12}$$

Based on these equations, the modeling aims to verify the accuracy of the model for a machine with a large diameter. Appendix A details the interface conditions and the equations employed to determine the unknown coefficients.

Evaluation of a generator's performance takes into account its parameters previously determined in [12]; moreover, iron-loss estimation is also considered according to [11]. After determining the flux densities' components, the Maxwell stress tensor method provides the electromagnetic torque, according to [20].

2.3. FEM Simulation

The FEM performs simulations aiming to obtain the electromagnetic performance in a 2D model using the software ANSYS Electronics. The simulations connect resistive loads to the model and provide the waveforms of back EMF, and the current and electromagnetic torque obtained by the virtual work method. Table 1 shows the main parameters of the model evaluated.

2.4. Prototype Structure

To simulate the real operation conditions of wind speed, a prototype structure with the same dimensions of the shrouded wind turbine driven by a motor provides the rotation and torque expected in Figure 2, as shown in Figure 5. The wooden structure identified as Number 1 in Figure 5a has the same dimensions of the wind turbine and the structure. Number 2 provides the support to the stator modules fixation with the same diffuser dimensions.

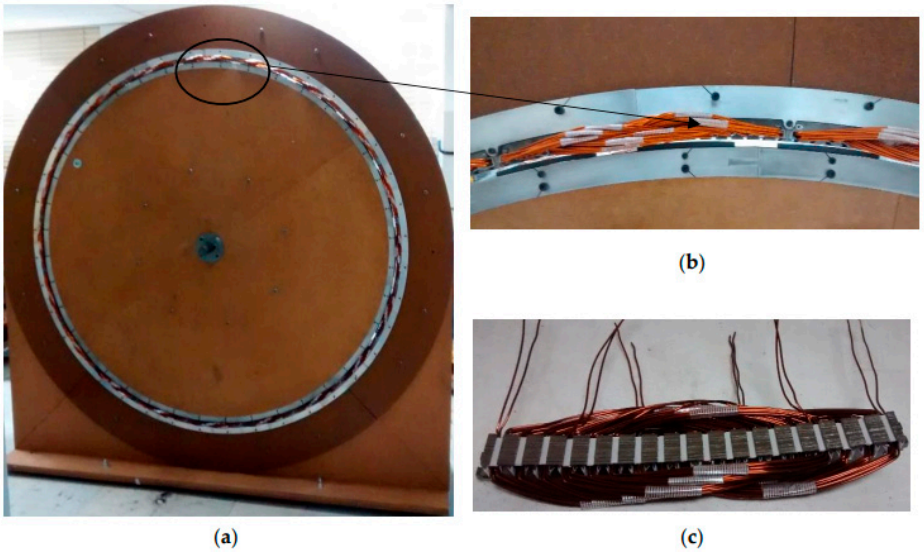

Figure 5. (**a**) Prototype structure of the stator modular ring generator; (**b**) one stator module; (**c**) detail of the assembly of rotor and stator.

Measurements of mechanical torque, terminal voltage and current under several rotation speeds provide the generator performance for no-load and on-load conditions for the wind speed range of the shrouded wind turbine. In addition, static measurements of the radial component flux density in the air gap with no load condition allow verifying directly the magnets' flux density and validating the analytical model and FEM results.

3. Results and Discussion

As aforementioned, static measurements with no current in the windings provide the radial component of magnetic flux density, and Figure 6 shows the comparison between experimental measurements, and analytical modeling and FEM results.

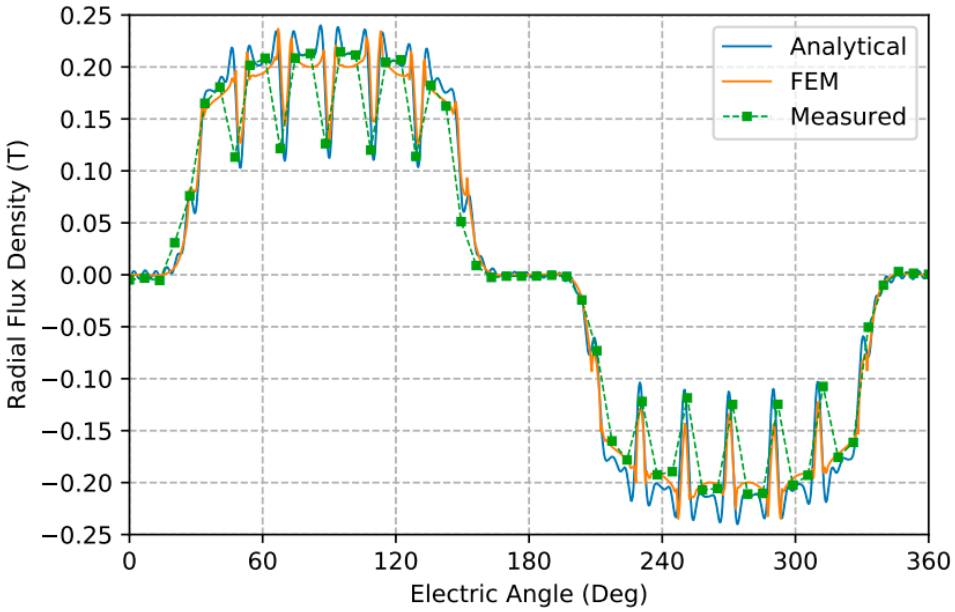

Figure 6. Analytical and finite element method (FEM) waveforms and experimental measurements of the radial component of the magnetic flux density at $r = R_S - 0.5$ mm.

Figure 6 aids in validating the analytical model and FEM results; both methods applied over a pair pole have good agreement to the experimental measurements, including the opening slots, where the biggest difference is approximately 21 mT. Concerning the air-gap magnitude of flux density, it is important to remember that due to the relation between the rotor diameter and rotation, the number of poles produces frequencies that increase expressively the stator iron losses. Thus, to reduce these losses, a lower flux density provided by ferrite magnets decreases the stator loss, also the back-iron length and the rotor height. Despite the impossibility of measuring directly the circumferential component of the magnetic flux density, Figure 7 presents the results of analytical modeling and FEM to verify the first one accurately; this component is also necessary to torque calculation using the Maxwell stress tensor method.

Although there are differences between the peak values due to the slots opening, both waveforms show good agreement regarding shape. However, it is important to highlight that the analytical model uses 1470 harmonics in the air-gap subdomain to achieve this precision. This number of harmonics is necessary due to the diameter rotor being bigger than the models previously presented, and a higher number of harmonics does not improve the accuracy or the ripple in the waveform.

To identify the stator loss caused by the magnet flux density, Figure 8 shows the torque measures with and without stator and the modules' stator iron loss along the work range.

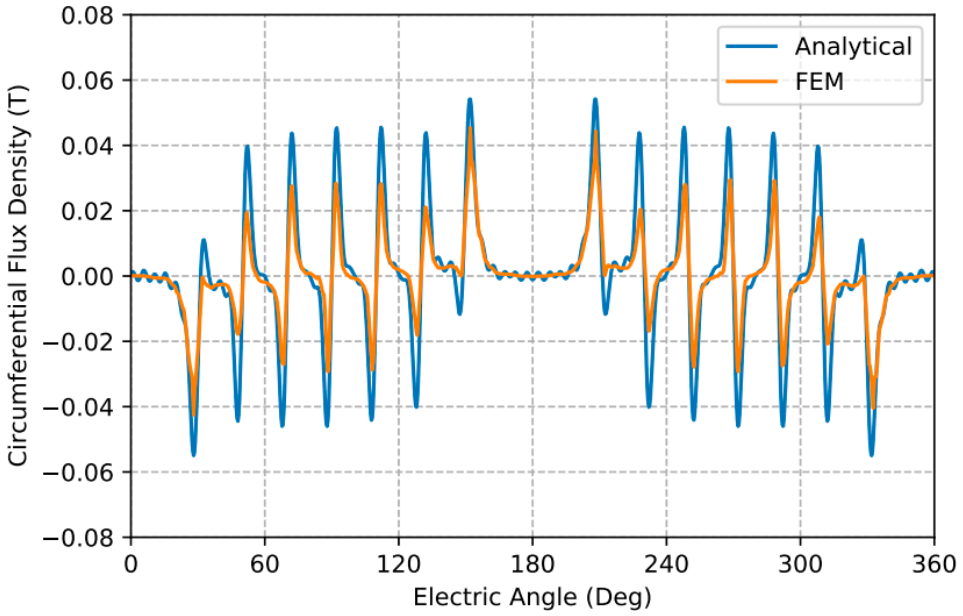

Figure 7. Analytical and FEM waveforms of circumferential component of magnetic flux density at $r = R_S - 1.0$ mm.

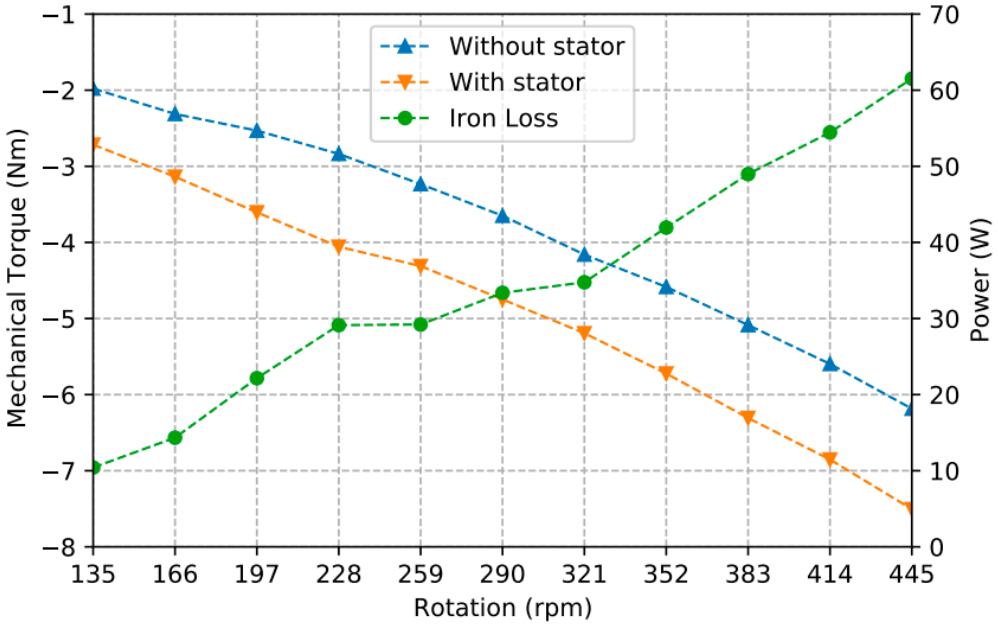

Figure 8. Average measured torque values with and without stator and module stator iron loss.

Considering the weight of the rotor, it is necessary to measure the torque produced by the friction between the axis and the bearings without the stator modules. Thus, the difference between measured torque with and without the stator modules provides the iron losses of the stator, as shown in Figure 8. As expected, the iron losses increase with the speed rotation, and considering the turbine power at the initial operation speed, it is possible to verify the importance of reducing the iron loss. Figure 8 presents some points that are not in good agreement with this behavior, because the adapted structure for the tests presented some vibration at the stator part that affected the torque measurements. However, it is important to highlight that the mechanical behavior of the real shrouded wind turbine is different, thus mitigating this problem.

Figures 9 and 10 show the terminal voltage comparison of waveform rms values under no-load and on-load conditions with the analytical model and FEM results, and experimental measurements.

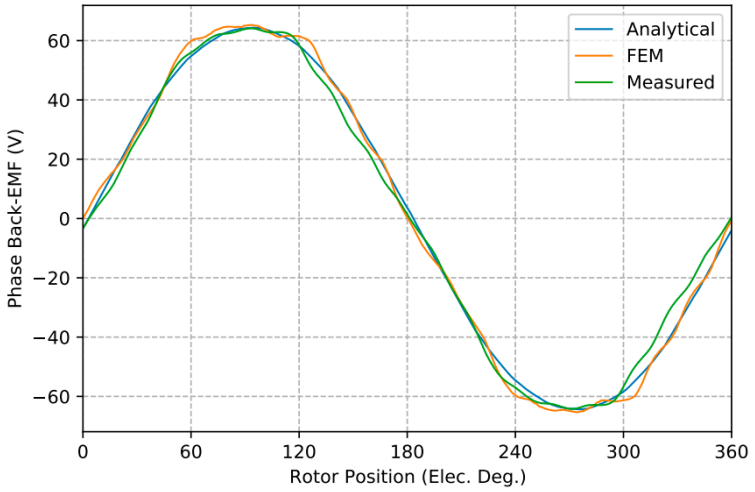

Figure 9. Waveform of phase back EMF for no-load conditions at 445 rpm.

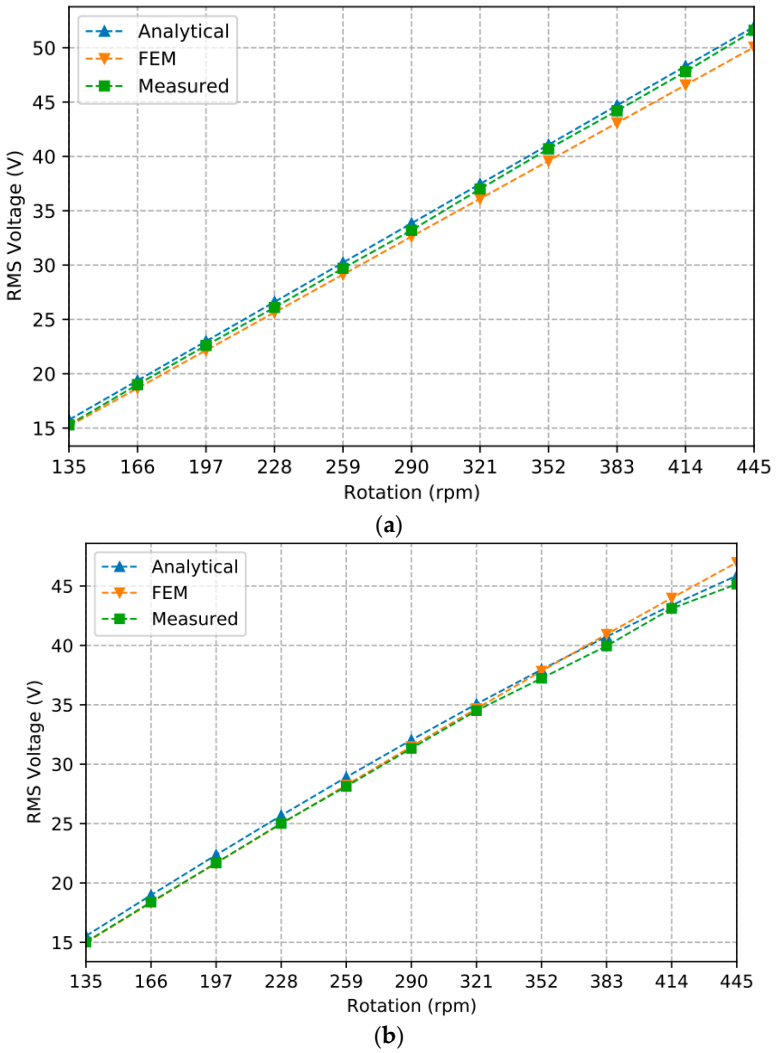

Figure 10. Terminal rms voltage for: (**a**) no-load; (**b**) on-load.

Results of Figure 9 confirm the validation of the radial component of the magnetic flux density as in Figure 6, and Figure 10 shows that the differences between the analytical method, FEM and experimental measurements are lower than approximately 4%. The comparison between the terminal rms voltages shows a voltage drop at the on-load condition, but the voltage behavior remains linear in both cases, which indicates that the armature reaction is not affecting the permanent magnets.

The rms current and copper loss in armature winding presented in Figure 11 allows the comparison of experimental measurements and analytical modeling and FEM.

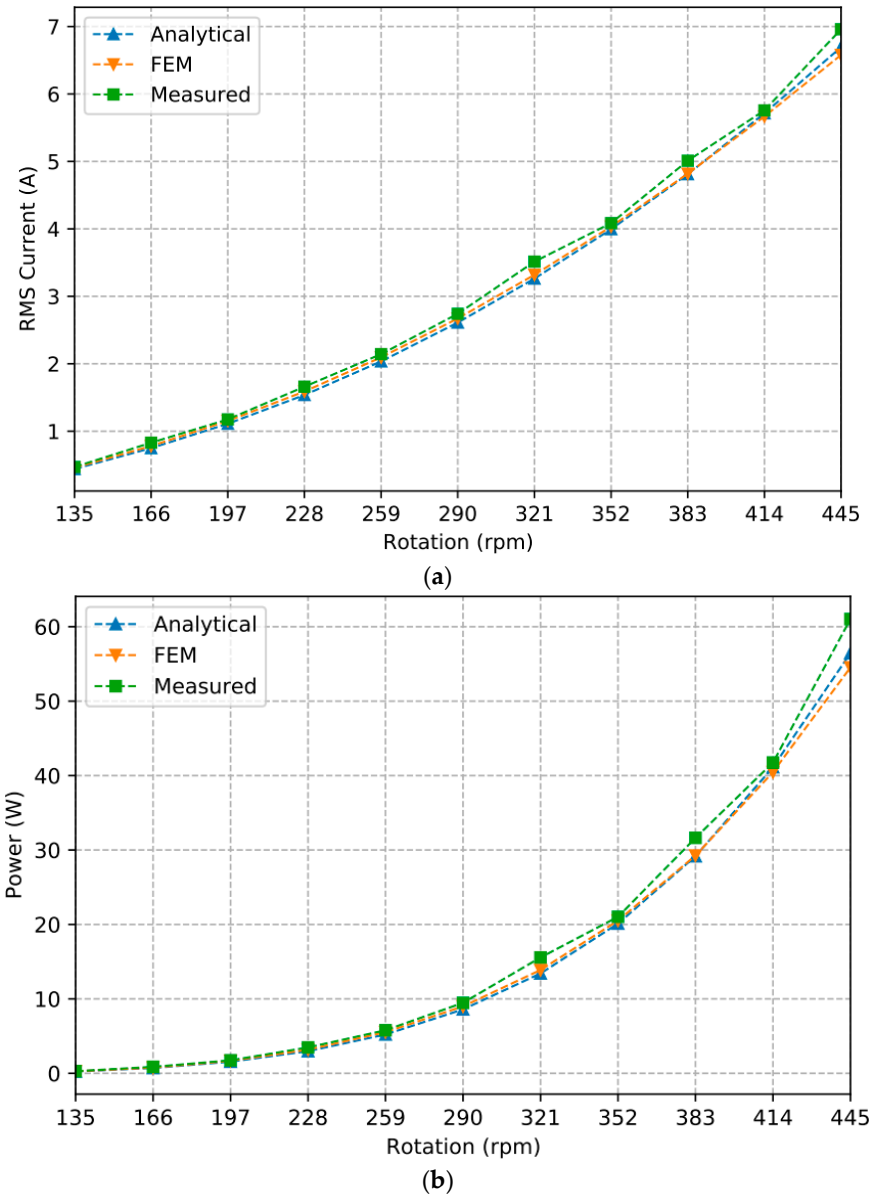

Figure 11. (**a**) current rms; (**b**) copper loss in armature winding.

The results for the rms current, as well as the voltage, lead to a validation of the analytical method and FEM. By comparing the copper loss to the iron loss, it is possible to conclude that due to the behavior of the first one, the iron loss is more significant to the generator's efficiency; only at the maximum speed are both approximately equal in magnitude.

According to the rms values for terminal voltage and current, Figure 12 shows the comparison of the load power along the work range.

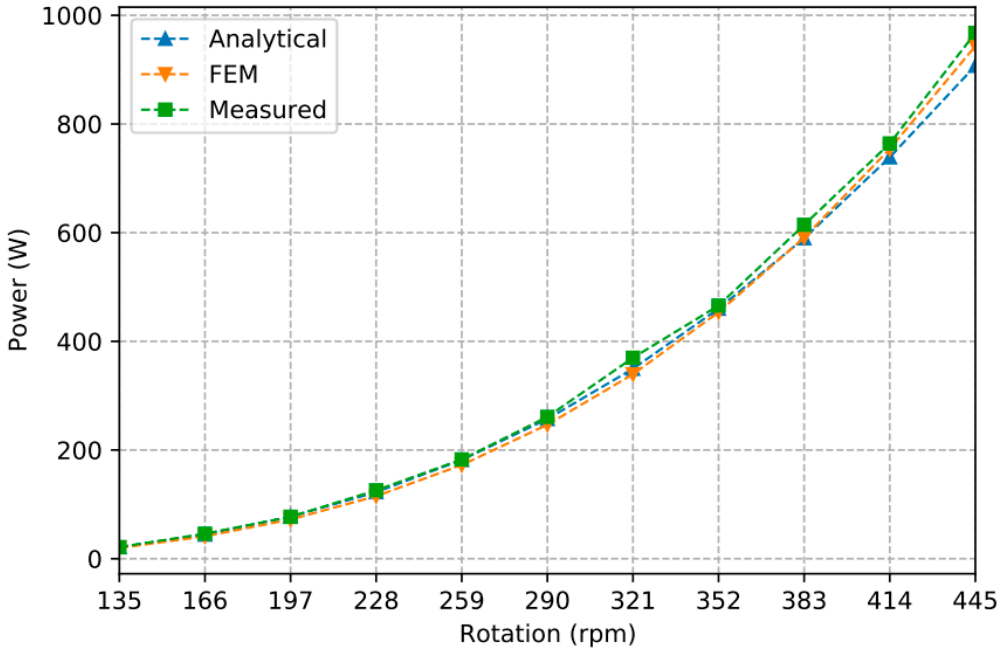

Figure 12. Mean values of power for resistive load.

As aforementioned, the load power results for the three methods present differences lower than approximately 6% and are below the turbine power presented in Figure 2 due to the iron loss and copper loss. The electromagnetic torque comparison presented in Figure 13 allows verifying the accuracy of the analytical modeling obtained by the Maxwell stress tensor and the FEM calculated with the aid of the virtual work method in comparison to the experimental measurements. The electromagnetic torque, experimental measurements and the no-load torque are presented in Figure 8.

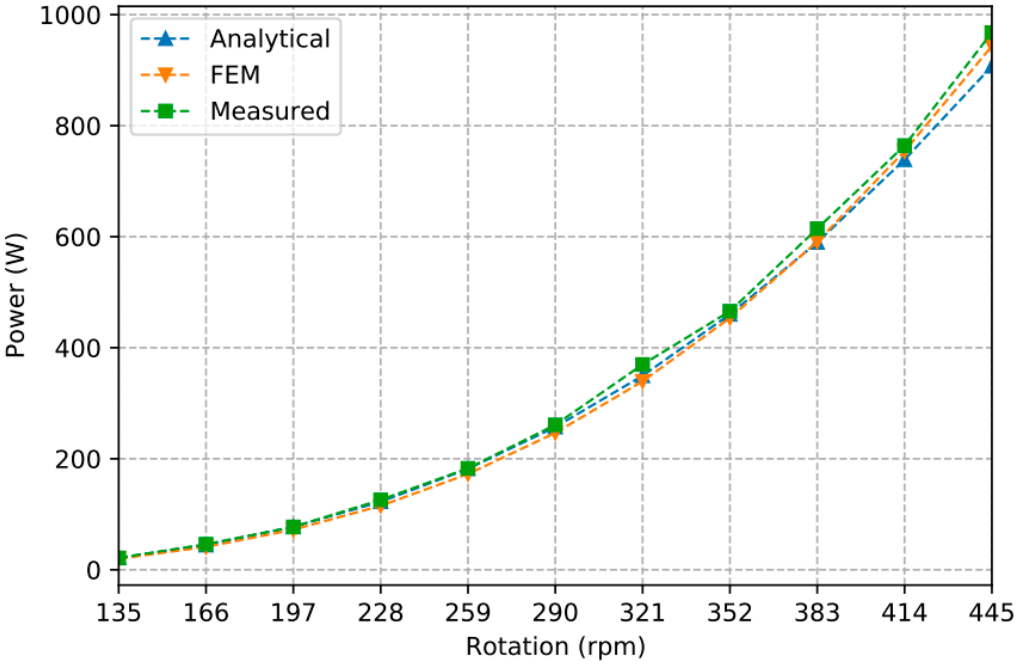

Figure 13. Average values of electromagnetic torque over the work range.

The results in Figure 13 show that despite the differences verified in the circumferential component of the magnetic flux density, both the Maxwell stress tensor and the virtual work method agree with the experimental measurements, with differences lower than

approximately 6.8%. This means that although a ripple exists in the circumferential component of the magnetic flux density, the analytical method for this dimension of machine can provide valid results. Lastly, Figure 14 shows an estimation of the generator's efficiency using the results of Figures 2 and 12.

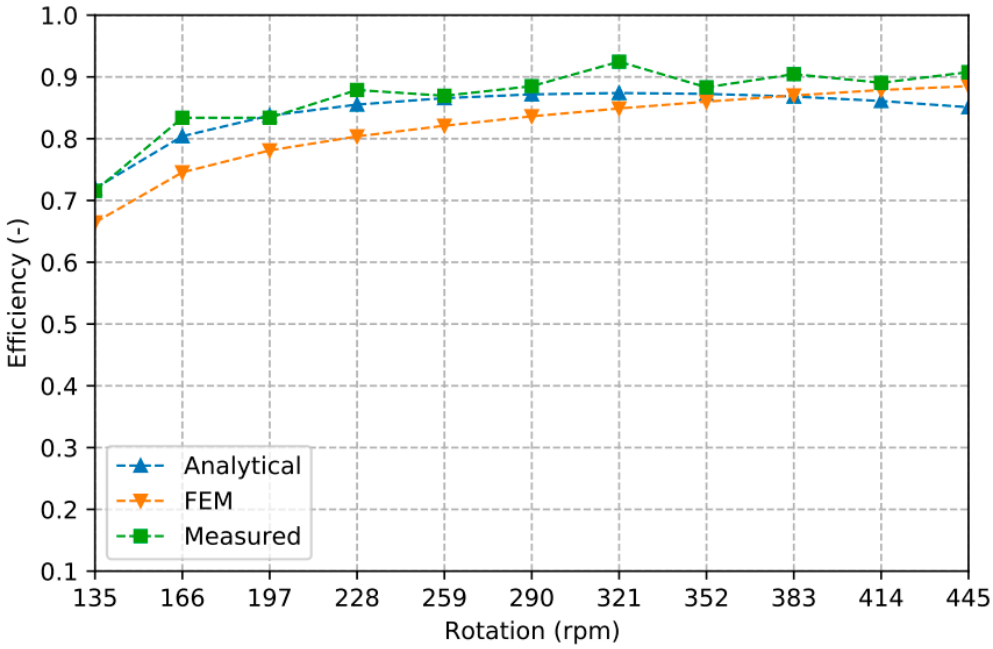

Figure 14. Estimation of the stator modular ring generator efficiency over the work range.

Figure 14 shows slight differences between the efficiencies that come from the combined uncertainties of the torque, speed, voltage and current used to calculate the efficiency, but overall, they all present a similar behavior, with a measured efficiency approximately equal to 90% for a good range of the turbine operation.

4. Conclusions

This paper evaluated the performance of a stator modular ring generator for wind-generation purposes using an analytical model, FEM and experimental measurements. Previous work used the analytical model employed at the analysis of this prototype; however, none of them had such huge a rotor diameter as compared to its axial length. The results showed that despite the large number of harmonics considered by the analytical modeling, its results were in good agreement with FEM and experimental measurements. Moreover, both the electromagnetic torque obtained by the virtual work method as well as the Maxwell stress tensor presented results quite similar to the experimental measurements, confirming the accuracy of both methods. The comparison between the prototype losses allowed verifying that the iron loss was more significant over most of the work range, due to the high number of poles and the rotation. Lastly, an efficiency evaluation showed similar behavior in all the methods, reaching approximately 90% in the work range with the highest values for the wind turbine power.

The next stage of the research is to assemble the stator modular ring generator to the shrouded wind turbine to evaluate the performance and verify the structural conditions regarding safety during operation. Thus, from these tests, results could be obtained that would allow the development of larger wind generators.

Author Contributions: J.A.O. developed the methods analysis, experimental measurements and wrote the article. Á.F.F.F. proposed the idea and guided the project development. All authors have read and agreed to the published version of the manuscript.

Funding: This research was funded by the Brazilian National Research Council, CNPq, by means of grant number 406809/2013-5.

Conflicts of Interest: The authors declare no conflict of interest.

Appendix A

Appendix A.1. Components of the Magnetic Flux Density

The components of the magnetic flux-density equations in region 1 according to Figure 3 are the following:

$$B_{r1} = -A_{11}\frac{m}{r}\left(r^m + \frac{R_r^{2m}}{r^m}\right)\sin(m\theta) + \left[C_{11}\frac{m}{r}\left(r^m + \frac{R_r^{2m}}{r^m}\right) + \frac{G_M}{m}\right]\cos(m\theta) \tag{A1}$$

$$B_{\theta 1} = \frac{m}{r}\left\{-A_{11}\left(r^m - \frac{R_r^{2m}}{r^m}\right)\cos(m\theta) - \left[C_{11}\left(r^m - \frac{R_r^{2m}}{r^m}\right) + \frac{G_M}{m}\right]\sin(m\theta)\right\} \tag{A2}$$

where

$$G_M = \frac{\mu_0 i_c}{\pi a^m}\left(r^m + \frac{R_r^{2m}}{r^m}\right)\sin(m\zeta) \tag{A3}$$

The components of the magnetic flux density in region 2 according to Figure 3 are

$$B_{r2i} = -\frac{E_n}{r}\left(A_{21}r^{E_n} + \frac{B_{21}}{r^{E_n}}\right)\sin\left(E_n\left(\theta + \frac{b_{oa}}{2} - \theta_i\right)\right) \tag{A4}$$

$$B_{\theta 2i} = -\frac{B_{20}}{r} - \frac{E_n}{r}\left(A_{21}r^{E_n} - \frac{B_{21}}{r^{E_n}}\right)\cos\left(E_n\left(\theta + \frac{b_{oa}}{2} - \theta_i\right)\right) \tag{A5}$$

and the components of the magnetic flux density in region 3 according to Figure 3 are

$$B_{r3i} = -\frac{E_k}{r}\left[A_{31}\left(r^{E_k} + \frac{R_{sb}^{2E_k}}{r^{E_k}}\right) + \frac{\mu_0 J_k}{E_k^2 - 4}\left(r^2 + \frac{2R_{sb}^{2+E_k}}{E_k^2 - 4}\right)\right]\sin\left(E_k\left(\theta + \frac{b_{sa}}{2} - \theta_i\right)\right) \tag{A6}$$

$$\begin{aligned} B_{\theta 3i} = &-\frac{\mu_0 J_0}{2}\left(\frac{R_{sb}^2}{r} - r\right) \\ &-\left[A_{31}\frac{E_k}{r}\left(r^{E_k} - \frac{R_{sb}^{2E_k}}{r^{E_k}}\right)\right. \\ &\left.+\frac{\mu_0 J_k}{E_k^2 - 4}\left(2r - \frac{2R_{sb}^{E_k+2}}{r^{E_k+1}}\right)\right]\cos\left(E_k\left(\theta + \frac{b_{sa}}{2} - \theta_i\right)\right) \end{aligned} \tag{A7}$$

where

$$J_0 = \frac{2Jd}{b_{sa}} \tag{A8}$$

$$J_k = \frac{2J}{k\pi}\sin\left(\frac{k\pi d}{b_{sa}}\right) \tag{A9}$$

where J is the current density through the windings coil.

Appendix A.2. Interface Conditions

Appendix A.2.1. Interface between Air Gap and Slot Opening

The magnetic flux-density condition along this interface is

$$B_{\theta 1}|_{r=R_s} = B_{\theta 2s} \tag{A10}$$

The expansion into Fourier series of the circumferential component of the magnetic flux density of region 2 is

$$B_{\theta 2s} = \sum_m C_s \cos(m\theta) + D_s \sin(m\theta) \tag{A11}$$

where

$$C_s = \sum_i \sum_m B_{\theta 2m} \eta_i + \sum_i B_{\theta 20} \eta_{i0} \tag{A12}$$

$$D_s = \sum_i \sum_m B_{\theta 2m} \gamma_i + \sum_i B_{\theta 20} \gamma_{i0} \tag{A13}$$

where

$$B_{\theta 20} = -\frac{B_{20}}{R_s} \tag{A14}$$

$$B_{\theta 2m} = -\frac{E_n}{R_s}\left(A_{21} R_s^{E_n} - \frac{B_{21}}{R_s^{E_n}}\right) \tag{A15}$$

and

$$\eta_i(m,n) = -\frac{m}{\pi(E_n^2 - m^2)}\left\{\cos(n\pi)\sin\left[m\left(\theta_i + \frac{b_{oa}}{2}\right)\right] - \sin\left[m\left(\theta_i - \frac{b_{oa}}{2}\right)\right]\right\} \tag{A16}$$

$$\eta_{i0}(m) = \frac{2}{m\pi}\sin\left(\frac{m b_{oa}}{2}\right)\cos(m\theta_i) \tag{A17}$$

$$\gamma_i(m,n) = \frac{m}{\pi(E_n^2 - m^2)}\left\{\cos(n\pi)\cos\left[m\left(\theta_i + \frac{b_{oa}}{2}\right)\right] - \cos\left[m\left(\theta_i - \frac{b_{oa}}{2}\right)\right]\right\} \tag{A18}$$

$$\gamma_{i0}(m) = \frac{2}{m\pi}\sin\left(\frac{m b_{oa}}{2}\right)\sin(m\theta_i) \tag{A19}$$

The circumferential component of the magnetic flux density of region 1 along the stator inner diameter is given by

$$B_{\theta 1}|_{r=R_s} = \frac{m}{R_s}\left\{-A_{11} G_1 \cos(m\theta) - \left[C_{11} G_1 + \frac{G_{M1}}{m}\right]\sin(m\theta)\right\} \tag{A20}$$

where

$$G_1 = R_s^m - \frac{R_r^{2m}}{R_s^m} \tag{A21}$$

$$G_{M1} = \frac{\mu_0 i_c}{\pi a^m} G_1 \sin(m\zeta) \tag{A22}$$

According to (A11) and (A20) the following expressions are obtained:

$$\begin{cases} -mA_{11}G_1 = R_s C_s \\ -mC_{11}G_1 + G_{M1} = R_s D_s \end{cases} \tag{A23}$$

The other condition in this interface is

$$A_{z1s} = A_{z2i}|_{r=R_s} \tag{A24}$$

The vector potential of region 1 along the stator inner diameter is expressed as

$$A_{z1}|_{r=R_s} = \sum_m [A_{1c}\cos(m\theta) + A_{1s}\sin(m\theta)] \tag{A25}$$

where

$$A_{1c} = A_{11} G_2 \tag{A26}$$

$$A_{1s} = C_{11}G_2 + \frac{G_{M2}}{m} \tag{A27}$$

and

$$G_2 = R_s^m + \frac{R_r^{2m}}{R_s^m} \tag{A28}$$

$$G_{M2} = \frac{\mu_0 i_c}{\pi a^m} G_2 \sin(m\zeta) \tag{A29}$$

To calculate Equation (A24) and (A25) must be expanded into Fourier series over the slot opening

$$A_{z1s} = A_{z10} + \sum_n A_{z1n} \cos\left[E_n\left(\theta + \frac{b_{oa}}{2} - \theta_i\right)\right] \tag{A30}$$

for $\theta_i - b_{oa}/2 \leq \theta \leq \theta_i + b_{oa}/2$, where

$$A_{z10} = \sum_m (A_{1c}\sigma_{i0} + A_{1s}\tau_{i0}) \tag{A31}$$

$$A_{z1n} = \sum_m (A_{1c}\sigma_{in} + A_{1s}\tau_{in}) \tag{A32}$$

and where

$$\sigma_{i0}(m) = \frac{\pi}{b_{oa}}\eta_{i0}(m) \tag{A33}$$

$$\tau_{i0}(m) = \frac{\pi}{b_{oa}}\gamma_{i0}(m) \tag{A34}$$

$$\sigma_{in}(n,m) = \frac{2\pi}{b_{oa}}\eta_{in}(m,n) \tag{A35}$$

$$\tau_{in}(n,m) = \frac{2\pi}{b_{oa}}\gamma_{in}(m,n) \tag{A36}$$

The vector potential at the opening slot region along the stator inner diameter is given by

$$A_{z2i}|_{r=R_s} = A_{20} + B_{20}\ln R_s + \left(A_{21}R_s^{E_n} + \frac{B_{21}}{R_s^{E_n}}\right)\cos\left[E_n\left(\theta + \frac{b_{oa}}{2} - \theta_i\right)\right] \tag{A37}$$

According to Equations (A30) and (A37), the following expressions are obtained:

$$\begin{cases} A_{1c}\sigma_{i0} + A_{1s}\tau_{i0} = A_{20} + B_{20}\ln R_s \\ A_{1c}\sigma_{in} + A_{1s}\tau_{in} = A_{21}R_s^{E_n} + B_{21}R_s^{-E_n} \end{cases} \tag{A38}$$

Appendix A.2.2. Interface between Slot Opening and Slot Region

The magnetic flux-density condition along this interface is

$$B_{\theta 2t} = B_{\theta 3t}|_{r=R_t} \tag{A39}$$

The expansion into Fourier series of the circumferential component of the magnetic flux density of region 2 along this interface is

$$B_{\theta 2t} = B_{\theta 0t}\omega_0 + \sum_k [B_{\theta 0t}\omega_{i0} + B_{\theta 2k}\omega_{ik}]\cos\left[E_k\left(\theta + \frac{b_{sa}}{2} - \theta_i\right)\right] \tag{A40}$$

where

$$B_{\theta 0t} = -\frac{B_{20}}{R_t} \tag{A41}$$

$$B_{\theta 2k} = -\frac{E_n}{R_t}\left(A_{21}R_t^{E_n} - \frac{B_{21}}{R_t^{E_n}}\right) \tag{A42}$$

$$\omega_0 = \frac{b_{oa}}{b_{sa}} \tag{A43}$$

$$\omega_{i0}(k) = \frac{4}{k\pi}\left[\sin\left(\frac{E_k b_{oa}}{2}\right)\cos\left(\frac{k\pi}{2}\right)\right] \tag{A44}$$

$$\omega_{ik}(k,n) = -\frac{2}{b_{sa}}\frac{E_k}{E_n^2 - E_k^2}\left\{\cos(n\pi)\sin\left[E_k\left(\frac{b_{sa}+b_{oa}}{2}\right)\right] - \sin\left[E_k\left(\frac{b_{sa}-b_{oa}}{2}\right)\right]\right\} \tag{A45}$$

The circumferential component of the magnetic flux density of region 3 along the slot inner diameter can be obtained as

$$B_{\theta 3t}|_{r=R_t} = B_{\theta 30} + \sum_k B_{\theta 3k}\cos\left[E_k\left(\theta + \frac{b_{sa}}{2} - \theta_i\right)\right] \tag{A46}$$

where

$$B_{\theta 30} = -\frac{\mu_0 J_0}{4}\left(\frac{2R_{sb}^2}{R_t} - 2R_t\right) \tag{A47}$$

$$B_{\theta 3k} = -A_{31}\frac{E_k}{R_t}\left(R_t^{E_k} - \frac{R_{sb}^{2E_k}}{R_t^{E_k}}\right) - \frac{\mu_0 J_k}{E_k^2 - 4}\left(2R_t - \frac{2R_{sb}^{E_k+2}}{R_t^{E_k+1}}\right) \tag{A48}$$

According to Equations (A39), (A40) and (A46) the following expressions are obtained:

$$\begin{cases} B_{\theta 0t}\omega_0 = B_{\theta 30} \\ B_{\theta 0t}\omega_{i0} + B_{\theta 2k}\omega_{ik} = B_{\theta 3k} \end{cases} \tag{A49}$$

The vector potential condition along this interface is

$$A_{z2i}|_{r=R_t} = A_{z3t} \tag{A50}$$

The expansion into Fourier series of the vector potential of region 3 along this interface is

$$A_{z3t} = A_{z30} + A_{z30}\xi_0 \sum_n A_{z3n}\xi_{in}\cos\left[E_n\left(\theta + \frac{b_{oa}}{2} - \theta_i\right)\right] \tag{A51}$$

where

$$A_{z30} = A_{30} + \frac{\mu_0 J_0}{4}\left(2R_{sb}^2 \ln R_t - R_t^2\right) \tag{A52}$$

$$A_{z3n} = A_{31}\left(R_t^{E_k} + \frac{R_{sb}^{2E_k}}{R_t^{E_k}}\right) + \frac{\mu_0 J_k}{E_k^2 - 4}\left(R_t^2 + \frac{2R_{sb}^{E_k+2}}{E_k R_t^{E_k}}\right) \tag{A53}$$

$$\xi_0(k) = \frac{b_{sa}}{2b_{oa}}\omega_{i0}(k) \tag{A54}$$

$$\xi_{in}(n,k) = \frac{b_{sa}}{b_{oa}}\omega_{in}(k,n) \tag{A55}$$

The vector potential of region 2 along the slot inner diameter can be obtained as

$$A_{z2i}|_{r=R_t} = A_{20} + B_{20}\ln R_t + \left(A_{21}R_t^{E_n} + \frac{B_{21}}{R_t^{E_n}}\right)\cos\left[E_n\left(\theta + \frac{b_{oa}}{2} - \theta_i\right)\right] \tag{A56}$$

According to Equations (A51) and (A56), the following expressions are obtained

$$\begin{cases} A_{20} + B_{20}\ln R_t = A_{z30} + A_{z30}\xi_0 \\ A_{21}R_t^{E_n} + \frac{B_{21}}{R_t^{E_n}} = A_{z3n}\xi_{in} \end{cases} \tag{A57}$$

Combining Equations (A23), (A38), (A49) and (A57) into a matrix, the unknowns in the components of the flux density can be determined.

References

1. Dilimulati, A.; Stathopoulos, T.; Paraschivoiu, M. Wind turbine designs for urban applications: A case study of shrouded diffuser casing for turbines. *J. Wind Eng. Ind. Aerodyn.* **2018**, *175*, 179–192. [CrossRef]
2. Ohya, Y.; Karasudani, T.; Sakurai, A.; Abe, K.; Inoue, M. Development of a shrouded wind turbine with a flanged diffuser. *J. Wind Eng. Ind. Aerodyn.* **2008**, *96*, 524–539. [CrossRef]
3. Ohya, Y.; Karasudani, T. A shrouded wind turbine generating high output power with wind-lens technology. *Energies* **2010**, *3*, 634–649. [CrossRef]
4. Verdum, V.; Homrich, R.P.; Flores Filho, A.F.; Dorrell, D.G. Ironless Machine Design for Wind-Based Microgeneration. *IEEE Trans. Magn.* **2017**, *53*, 1–4. [CrossRef]
5. Spooner, E.; Williamson, A.C.; Catto, G. Modular design of permanent-magnet generators for wind turbines. *IEE Proc. Electr. Power Appl.* **1996**, *143*, 388. [CrossRef]
6. Zhang, J.; Chen, Z.; Cheng, M. Design and comparison of a novel stator interior permanent magnet generator for direct-drive wind turbines. *IET Renew. Power Gener.* **2007**, *1*, 203–210. [CrossRef]
7. Ditmanson, C.; Hein, P.; Kolb, S.; Molck, J.; Bernet, S. A new modular flux-switching permanent-magnet drive for large wind turbines. *IEEE Trans. Ind. Appl.* **2014**, *50*, 3787–3794. [CrossRef]
8. Zhao, J.; Zheng, Y.; Zhu, C.; Liu, X.; Li, B. A novel modular-stator outer-rotor flux-switching permanent-magnet motor. *Energies* **2017**, *10*, 937. [CrossRef]
9. Li, Y.X.; Zhu, Z.Q.; Thomas, A.S.; Wu, Z.Y.; Wu, X.M. Novel Modular Fractional Slot Permanent Magnet Machines With Redundant Teeth. *IEEE Trans. Magn.* **2019**, *55*, 1–10. [CrossRef]
10. Petrov, I.; Di, C.; Lindh, P.; Niemela, M.; Repo, A.K.; Pyrhonen, J. Fault-tolerant modular stator concentrated winding permanent magnet machine. *IEEE Access* **2020**, *8*, 7806–7816. [CrossRef]
11. Oliveira, J.A.; Filho, A.F.F.; Dorrell, D.G. Ring-shaped surface-mounted permanent magnet generators with modular stator for small wind turbines. In Proceedings of the 2018 IEEE International Magnetics Conference (INTERMAG), Singapore, 23–27 April 2018; pp. 1–5. [CrossRef]
12. Oliveira, J.A.; Filho, A.F.F. Parameters evaluation of a permanent magnet synchronous generator with modular stator. *IEEE Lat. Am. Trans.* **2019**, *17*, 1678–1685. [CrossRef]
13. Lubin, T.; Mezani, S.; Rezzoug, A. 2D Exact Analytical Model for Surface-Mounted Permanent Magnet Motors with Semi-Closed Slots. *IEEE Trans. Magn.* **2011**, *2*, 1–15.
14. Wu, L.J.; Zhu, Z.Q.; Staton, D.; Popescu, M.; Hawkins, D. Analytical prediction of electromagnetic performance of surface-mounted PM machines based on subdomain model accounting for tooth-tips. *IET Electr. Power Appl.* **2011**, *5*, 597. [CrossRef]
15. Boutora, Y.; Takorabet, N.; Ibtiouen, R. Analytical model on real geometries of magnet bars of surface permanent magnet slotless machine. *Prog. Electromagn. Res. B* **2016**, *66*, 31–47. [CrossRef]
16. Binns, K.J.; Lawrenson, P.J.; Trowbridge, C.W. *The Analytical and Numerical Solution of Electric and Magnetic Fields*; John Wiley & Sons: New York, NY, USA, 1993.
17. Zhou, Y.; Li, H.; Meng, G.; Zhou, S.; Cao, Q. Analytical calculation of magnetic field and cogging torque in surface-mounted permanent-magnet machines accounting for any eccentric rotor shape. *IEEE Trans. Ind. Electron.* **2015**, *62*, 3438–3447. [CrossRef]
18. Xue, Z.; Li, H.; Zhou, Y.; Ren, N.; Wen, W. Analytical Prediction and Optimization of Cogging Torque in Surface-Mounted Permanent Magnet Machines with Modified Particle Swarm Optimization. *IEEE Trans. Ind. Electron.* **2017**, *64*, 9795–9805. [CrossRef]
19. Wu, L.J.; Zhu, Z.Q.; Staton, D.; Popescu, M.; Hawkins, D. Subdomain model for predicting armature reaction field of surface-mounted permanent-magnet machines accounting for tooth-tips. *IEEE Trans. Magn.* **2012**, *48*, 107–117. [CrossRef]
20. Meessen, K.J.; Paulides, J.J.H.; Lomonova, E.A. Force calculations in 3-D cylindrical structures using fourier analysis and the maxwell stress tensor. *IEEE Trans. Magn.* **2013**, *49*, 536–545. [CrossRef]